Letter

Peierls transition driven ferroelasticity in the two-dimensional d-f hybrid magnets

Haipeng You, Yang Zhang [iD], Jun Chen, Ning Ding, Ming An, Lin Miao, and Shuai Dong [iD]*

School of Physics, Southeast University, Nanjing 211189, China

For broad nanoscale applications, it is crucial to implement more functional properties, especially ferroic orders, into two-dimensional materials. Here, GdI_3 is theoretically identified as a honeycomb antiferromagnet with a large $4f$ magnetic moment. The intercalation of metal atoms can dope electrons into Gd's $5d$ orbitals, which alters its magnetic state and leads to a Peierls transition. Due to strong electron-phonon coupling, the Peierls transition induces prominent ferroelasticity, making it a multiferroic system. The strain from unidirectional stretching can be self-relaxed via the resizing of triple ferroelastic domains, which can protect the magnet against mechanical breaking in flexible applications.

I. INTRODUCTION

Since the discovery of graphene, two-dimensional (2D) materials have formed a growing field, containing many semiconductors, semimetals, as well as topological materials, which have brought great opportunities for applications in microelectronics, optoelectronics, catalysis, etc., for their excellent physical and chemical properties. In fact, more functionalities can be implemented into 2D materials, which can provide superior performances than their three-dimensional (3D) counterparts. Very recently, 2D materials with intrinsic ferroic orders (e.g., magnetism or polarity) became an emerging branch of the 2D family, which are of great interest for spintronic/electronic applications in the nanoscale [1–5].

Currently, most studied ferromagnetic (FM) and antiferromagnetic (AFM) 2D materials originate from van der Waals (vdW) or MXene layered materials with transition metals (e.g., V, Cr, Mn, Fe, Co, Ni, Cu) [6–17], i.e., with $3d$-electron spins. In addition, $4f$ electrons, with an even stronger Hubbard correlation and more spatial localization, can also provide magnetic moments, but have been much less studied in 2D materials. The $4f$-electron magnets have some unique physical characteristics. For example, the spin-orbit coupling (SOC) is typically much stronger for $4f$ orbitals, which may lead to larger magnetocrystalline anisotropy, an important condition to stabilize magnetic orders in the 2D limit. Also, the maximum local spin moment can be larger than the $3d$ one. However, due to the localized distribution of $4f$ orbitals, the exchanges between neighboring $4f$ spins are typically weaker, leading to lower ordering temperatures.

Recently, a 2D monolayer with a rare-earth metal, GdI_2, was predicted to be a FM semiconductor with a Curie temperature (T_C) close to room temperature [18]. Its exotic large exchange interaction comes from the $4f^7 + 5d^1$ hybridization of Gd^{2+}. The spatially expanded $5d$ electron acts as a bridge to

couple localized $4f$ spins. This work opened a door to pursue high-performance 2D magnets based on $4f$ spins.

Here, another 2D f-electron halide, the GdI_3 monolayer, is theoretically studied. Different from the compact triangular structure of GdI_2, the GdI_3 monolayer possesses a honeycomb geometry of Gd^{3+} spins. The "vacancies" within the hex-atomic rings can host dopants, providing an efficient route to tune its physical properties. Indeed, here the magnetic ground state can be tuned by electron doping, accompanying the Peierls transition. Prominent ferroelasticity is induced by this Peierls transition. Thus, doped GdI_3 becomes a 2D multiferroic system with superior elasticity, adding an additional value to 2D magnetic materials.

II. METHODS

First-principles calculations are performed based on the spin-polarized density functional theory (DFT) implemented in the Vienna *ab initio* simulation package (VASP) code [19]. The projected augmented-wave (PAW) method is used to describe the ion-electron interaction, and the kinetic energy cutoff for the plane wave is set as 500 eV. The Perdew-Burke-Ernzerhof (PBE) parametrization of the generalized gradient approximation (GGA) is used for the exchange-correlation functional [20]. The Hubbard correlation is considered using the rotationally invariant GGA + U method introduced by Liechtenstein *et al.* [21], with $U = 9.2$ eV and $J = 1.2$ eV applied on Gd's $4f$ orbitals [22].

The structures are relaxed with the conjugate gradient method until the Hellmann-Feynman force on each atom is less than 0.01 eV/Å. The Monkhorst-Pack scheme is chosen to sample the Brillouin zone, with a $4 \times 4 \times 1$ k point for the primitive cell and $2 \times 2 \times 1$ for the supercell. For monolayers, a 20-Å vacuum layer is added to avoid interactions between adjacent layers. The vdW interaction is described by the DFT-D2 functional [23]. The phonon band structure is calculated using the density functional perturbation theory (DFPT) [24,25].

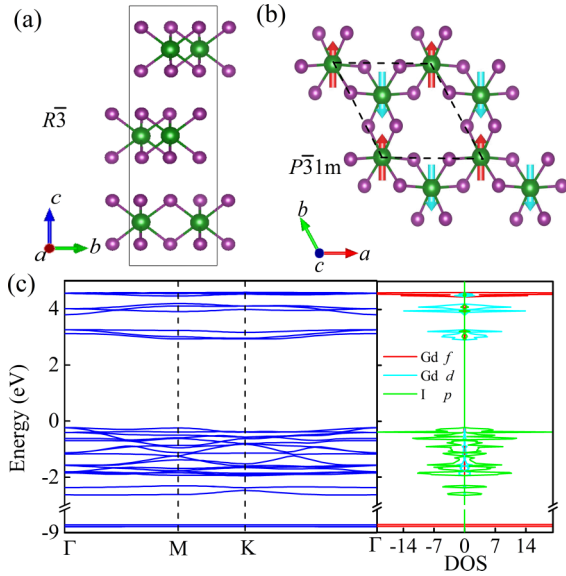*Corresponding author: sdong@seu.edu.cn

FIG. 1. Physical properties of GdI$_3$. (a) The structure of vdW layered GdI$_3$. (b) The top view of a monolayer exfoliated from the vdW layered phase. The primitive cell is indicated by the dashed lines. Green: Gd. Purple: I. The spins of the Néel-type antiferromagnetic (AFM) ground state are indicated by arrows. (c) The band structure and density of states (DOS) of the GdI$_3$ monolayer. The lowest conducting band is contributed by Gd's 5d orbitals, while the highest valence band is from I's 5p oribitals.

Spin-orbit coupling (SOC) is considered when calculating the magnetocrystalline anisotropy energy (MAE). The MAE coefficient K is also estimated as $E_c - E_a$, where E_x denotes the energy of the ferromagnetic state with spin pointing along the x direction.

III. RESULTS AND DISCUSSION

A. Physical properties of GdI$_3$

For GdI$_3$ bulk, there are two possible structures. One predicted phase for various RI$_3$ (R: a rare-earth metal such as Tb, Dy, Er, etc.) consists of vdW-coupled chains (with space group $P6_3/mmc$) [26], as shown in Fig. S1 of the Supplemental Material (SM) [27]. Another phase is a vdW layered structure with space group $R\bar{3}$, as shown in Fig. 1(a), which was synthesized experimentally more than half a century ago [28].

To clarify the ground state, both structures of $P6_3/mmc$ and $R\bar{3}$ phases are calculated for comparison. As summarized in Table S1 [27], our optimized lattice constants agree with the previous experiment [28], implying reliable results. According to our calculation, the energy of the $P6_3/mmc$ phase is 366 meV/f.u. higher than that of the $R\bar{3}$ phase, implying a more stable $R\bar{3}$ phase, in consistent with experimental observation. The calculated Gd's magnetic moment is very close to the expectation value 7μ_B/Gd, coming from its half-filled 4f orbitals, while the residual moment on the I ion is negligibly small.

For the $R\bar{3}$ GdI$_3$ bulk with 1T-BiI$_3$-type vdW layers, the I-Gd-I sandwich layers are stacked along the c axis in an ABC sequence. Each Gd ion is caged within the I octahedron,

while the neighbor octahedra connect via an edge-sharing manner [Fig. 1(b)], similar to the crystal structure of 1T-phase CrI$_3$ [1].

The GdI$_3$ monolayer can be exfoliated from its layered bulk. The exfoliation process is simulated to obtain the cleavage energy, as shown in Fig. S2 in SM [27]. Compared with the cleavage energy of graphite (0.37 J/m^2), GdI$_3$ has a smaller value (0.12 J/m^2), implying its easier exfoliation. Then, in the following, the GdI$_3$ monolayer will be calculated.

To investigate the magnetic ground state, the four most possible magnetic orders, i.e., ferromagnetic (FM) and three AFM ones (Néel, zigzag, and stripy, as shown in Fig. S3 in SM [27]), are considered [29]. According to our DFT calculation, the Néel-type AFM state [Fig. 1(b)] has the lowest energy, as compared in Table S2 in SM [27]. This Néel-type AFM state is expected since the half-filling 4f orbitals prefer the AFM coupling according to the Goodenough-Kanamori rule. The energy difference between the FM and Néel-type AFM states is only 1.8 meV/f.u. Such a weak exchange is reasonable considering the spatially localized 4f orbitals. Therefore, the expected Néel temperature (T_N) for the GdI$_3$ monolayer should be very low. The value of MAE is -0.03 meV/Gd, indicating an easy axis pointing out of plane. Such weak magnetic anisotropy is due to the half-filled 4f orbitals, which cancels the effect of SOC.

The electronic structure of the Néel-type AFM GdI$_3$ monolayer is shown in Fig. 1(c). It is a Mott insulator, with fully split narrow 4f bands, due to large Hubbard repulsion. The lowest conducting band is contributed by Gd's 5d orbitals, instead of 4f's upper Hubbard band. Also, the highest valence band is from I's 5p orbitals.

The low-temperature antiferromagnetism in GdI$_3$ is in sharp contrast with the predicted high-temperature ferromagnetism in GdI$_2$. Then it is interesting to explore the electron doping effect in GdI$_3$. Is it possible to achieve high-temperature ferromagnetism by electron doping? Is it possible to obtain a metal-insulator transition with electron doping? Is there any other emergent physics in doped systems, such as what happens in high-T_C superconducting cuprates and colossal magnetoresistive manganites [30]?

B. Peierls transition in Li-intercalated GdI$_3$

To answer these questions, Li atoms are intercalated into the interstitial positions of hexatomic rings, as shown in Fig. 2(a). Now the chemical formula of the monolayer becomes (GdI$_3$)$_2$Li, and the valence of Gd becomes fractional $+2.5$, which would be a source for emergent phenomena.

Then the structure of (GdI$_3$)$_2$Li is relaxed with the aforementioned four magnetic orders. As compared in Table I, the stripy-AFM state [Fig. 2(b)] possesses the lowest energy. The magnetic moment becomes ~7.5μ_B/Gd, as expected. The MAE coefficient K for (GdI$_3$)$_2$Li is estimated as 0.46 meV/Gd, which prefers the in-plane alignment of spins. The enhanced magnetic anisotropy is due to the strong SOC of Gd's partially filled 5d orbitals. Meanwhile, there is a strong lattice deformation, i.e., a Peierls-type dimerization, which reduces the symmetry from trigonal to monoclinic $C2/m$ (No. 12). There is a strong disproportion of the nearest-neighbor Gd-Gd distance d, which is seriously split into two
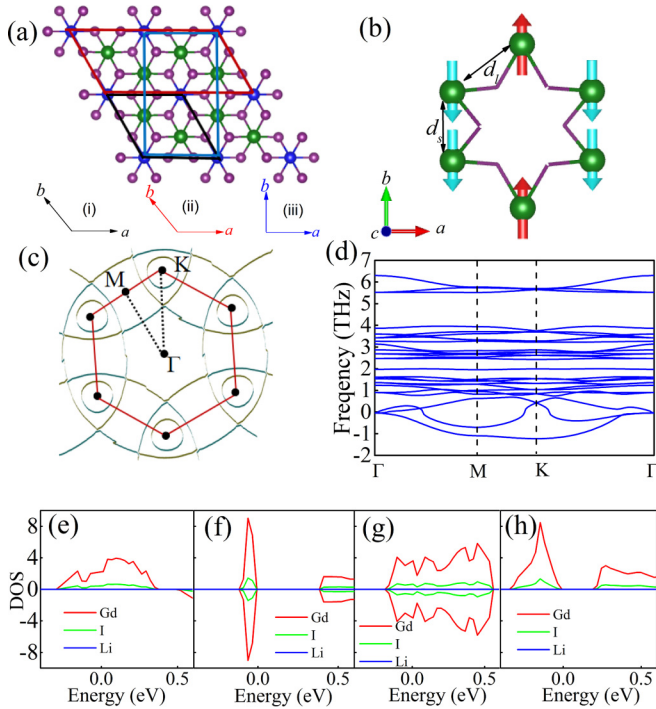
FIG. 2. The Peierls transition of $(GdI_3)_2Li$. (a) Structure of Li-implanted GdI_3 monolayer. Blue: Li. Black rhombus: Primitive cell of FM or Néel AFM states. Red parallelogram: Primitive cell of the zigzag-AFM state. Blue rectangle: Primitive cell of the stripy-AFM state. (b) The Gd framework for the stripy-AFM phase. The structural dimerization can be visualized clearly: the shorter d_s between parallel-spin Gd-Gd pairs and longer d_l between antiparallel-spin ones. (c) Fermi surface of the FM $P\bar{3}1m$ state, coming from Gd's $5d$ electrons. The hexagonal Fermi surface surrounding the Γ point provides the possibility for Fermi-surface nesting. (d) Phonon spectrum of the FM $P\bar{3}1m$ state, which indicates the dynamic instability. (e)–(h) Comparison of DOS near the Fermi level. (e) FM state on an optimized $P\bar{3}1m$ structure. (f) Stripy state on an optimized $C2/m$ structure. (g) Stripy state on a $P\bar{3}1m$ structure. (h) FM state on an optimized $C2/m$ structure.

types: longer d_l and shorter d_s, as indicated in Fig. 2(b) and listed in Table I.

This stripy antiferromagnetism and strong lattice deformation is nontrivial. A direct question is whether the lattice

TABLE I. Optimized structures of $(GdI_3)_2Li$ with different magnetic orders. Lattice constants (a and b) and nearest-neighbor Gd-Gd distances (d_l: longer one; d_s: shorter one) are in units of Å. The shapes of primitive cells can be found in Fig. 2(a). The energies are in units of meV/f.u. and the FM one with a highly symmetric structure is taken as the reference.

Order	Space group	Energy	a	b	d_l	d_s
FM	$P\bar{3}1m$	0	7.502		4.331	
Néel	$P\bar{3}1m$	93	7.503		4.332	
Zigzag	$C2/m$	5.5	7.438	7.678	4.592	4.207
Stripy	$C2/m$	−52.6	7.662	12.730	4.625	3.773
FM	$C2/m$	−49.9	7.680	12.726	4.639	3.761

deformation is driven by the magnetostriction effect since the stripy antiferromagnetism is also dimerized, or, in reverse, the stripy antiferromagnetism is driven by the lattice dimerization. To clarify the real origin, the Fermi surface and phonon spectrum of the highly symmetric FM state are analyzed. As shown in Fig. 2(c), there are small pockets around the K point. In addition, six large "circles" cross with each other and form a hexagon surrounding the Γ point, which provides the possibility for Fermi-surface nesting, i.e., the electronic driving force for the Peierls transition.

Accordingly, for the FM state with a highly symmetric structure, the imaginary frequencies of the phonon spectrum [Fig. 2(d)] also suggest a spontaneous structural instability. In fact, the optimized $C2/m$ structure with FM order leads to an even slightly larger disproportion between d_l and d_s, as listed in Table I. Thus, the appearance of lattice dimerization is not driven by the magnetostriction of stripy antiferromagnetism, but due to the instability of the electronic structure.

Peierls-type dimerization can tune the band structure, as compared in Figs. 2(e)–2(h). The FM state with an optimized $P\bar{3}1m$ structure is metallic [Fig. 2(e)], while the stripy state with an optimized $C2/m$ structure is a semiconductor. To further clarify the origin of the gap opening, the stripy-AFM order is imposed on the $P\bar{3}1m$ structure, which cannot open the band gap [Fig. 2(g)]. In contrast, the FM order on the $C2/m$ structure can open a band gap at the Fermi level [Fig. 3(h)].

Thus, it is unambiguous to conclude that the physical properties of $(GdI_3)_2Li$, including the lattice deformation, magnetic transition, and band gap opening, are all dominated by the Peierls-type transition. On one hand, with both optimized $C2/m$ structures, the energy differences between FM and stripy-AFM states are so small (2.7 meV/Gd higher for the FM state), implying a low Néel temperature. Considering the large magnetic moment ($7.5\mu_B$/Gd), the Zeeman energy gained from a moderate magnetic field $\sim$6.2 T can overcome the small energy difference and drive an AFM-FM phase transition. At finite temperature, the required magnetic field can be even lower with the help of thermal fluctuation. This magnetic transition can lead to negative magnetoresistance, considering the different band gaps of the FM phase (0.19 eV) and the stripy-AFM phase (0.38 eV), as compared between Figs. 2(f) and 2(h). On the other hand, the energy gain from lattice dimerization reaches 49.9 meV/Gd with the FM order, implying that the lattice dimerization should occur at a much higher temperature than the Néel temperature of stripy-AFM order.

Besides the magnetic transition, the Peierls transition can lead to an even more interesting physical phenomenon, i.e., ferroelasticity [31]. As stated before, the driving force of the Peierls transition is Gd's $5d$ electron, which can form a unidirectional charge density wave, as shown in Fig. 3(a). The $5d$ electrons mostly stay in the middle of the shorter Gd-Gd pair, while the middle of the longer Gd-Gd pair is almost empty, i.e., bond-centered charge ordering [32]. These electron spindles break the threefold rotational symmetry, and induce a shrunk lattice constant along the spindle direction, i.e., the b axis of the α domain as shown in Fig. 3(a). This ferroelastic deformation can reach 4%, comparable with the tetragonality of tetragonal $BaTiO_3$. The coexisting ferroelasticity and antiferromagnetism makes
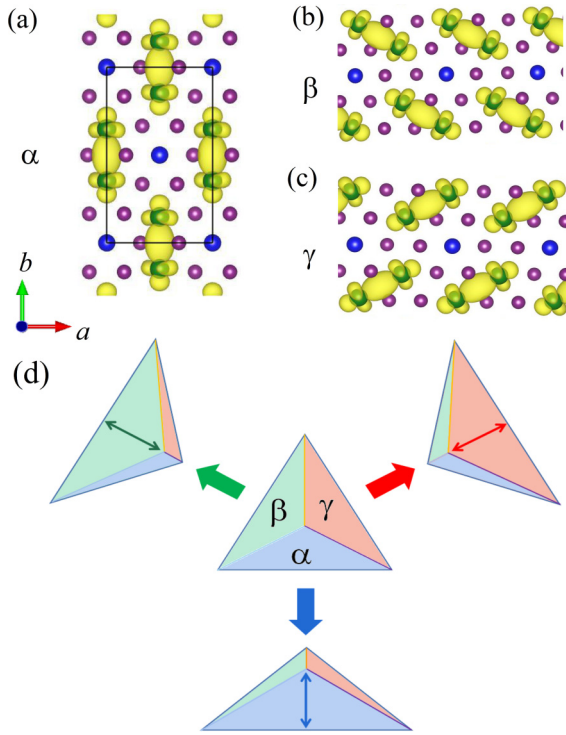
FIG. 3. (a) Schematic of electron distribution of Gd's $5d$ electrons. The electron spindles are along the b axis in this α domain. The associated ferroelasticity can be characterized by the b/a ratio of the black rectangle, which is 1.661, ~4% shorter than the original 1.732 for the $P\bar{3}1m$ phase. (b), (c) Two other ferroelastic domains with electron spindles along different directions, referred to as β and γ domains. (d) Origin of superelasticity. The macroscopic shape of the $(GdI_3)_2Li$ monolayer can be deformed by external forces. The inner strain can be relaxed to some extent by the rotation of electron spindles, i.e., the resizing of the corresponding ferroelastic domains.

$(GdI_3)_2Li$ a multiferroic system, although it does not contain ferroelectricity.

Furthermore, the threefold rotational symmetry of the parent phase allows the other two ferroelastic domains with different orientations of electron spindles, i.e., the β and γ domains, as shown in Figs. 3(b) and 3(c). Starting from an anisotropic state with the same amounts of α-β-γ domains [center of Fig. 3(d)], external forces along certain directions can tune the detailed balance among these triple ferroelastic domains. Then the change of ferroelastic domains can relax the inner strain by rotating these electron spindles, making the $(GdI_3)_2Li$ monolayer more elastic against mechanical damage in a certain range, which is crucial for flexible applications. Very recently, an experiment demonstrated the superelasticity of a free-standing ferroelectric $BaTiO_3$ membrane, which was attributed to the continuous electric dipole rotation [33]. In fact, it should be a common physical property of ferroelastics, not limited to ferroelectrics only, as demonstrated by the nonferroelectric but ferroelastic $(GdI_3)_2Li$ monolayer here.

C. Results of Mg-intercalated GdI_3

The above results have demonstrated some interesting physical properties of half-doped GdI_3, except for the ex-

TABLE II. Optimized structures of $(GdI_3)_2Mg$ with different magnetic orders. Lattice constants (a and b) and nearest-neighbor Gd-Gd distances (d_l: longer one; d_s: shorter one) are in units of Å. The energies are in units of meV/f.u. and the FM one with a highly symmetric structure is taken as the reference.

Order	Space group	Energy	a	b	d_l	d_s
FM	$P\bar{3}1m$	0	7.461		4.307	
Néel	$P\bar{3}1m$	139.9	7.511		4.336	
Zigzag	$C2/m$	−43.8	7.168	15.160	4.938	3.985
Stripy	$C2/m$	−129.3	7.877	12.416	4.834	3.404

pected high-temperature ferromagnetism. Then a natural question is whether one-electron intercalation can make GdI_3 more as GdI_2, namely to be a FM semiconductor. To answer this question, Mg intercalation is studied.

In $(GdI_3)_2Mg$, the valence of Gd becomes +2, identical to that in GdI_2. However, the stripy-AFM state remains the lowest-energy one, according to our DFT calculations, as compared in Table II. The magnetic moment becomes $\sim 8\mu_B/Gd$, as expected. The MAE coefficient K for $(GdI_3)_2Mg$ is estimated as 1.05 meV, which also prefers an in-plane alignment due to the SOC of Gd's $5d$ orbitals. The ferroelastic distortion is also prominent. In this sense, the Peierls transition remains the dominant factor, which opens a band gap at the Fermi level, as shown in Fig. 4(a) (and Fig. S4 in SM [27]).
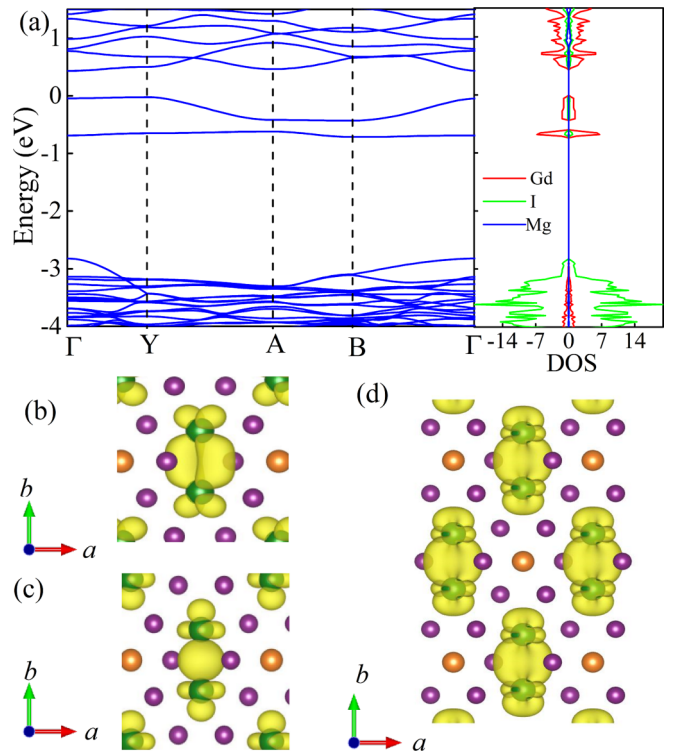

FIG. 4. Results of $(GdI_3)_2Mg$. (a) Electronic structure of the stripy-AFM state. The system remains a semiconductor, with two lowered $5d$ bands. Left: Band structure. Right: DOS. (b)–(d) Distribution of electrons. (b) and (c) are for two occupied $5d$ bands, respectively, and (d) are the total occupations.

How can the Peierls transition occur in the case of one-electron doping? It is due to the multiple orbitals of Gd's t_{2g} sector, which can separate one electron into a half occupation of two orbitals. Then the orbital-selective Peierls transition occurs (see Fig. S5 in SM [27]), similar to the orbital-selective Mott transition in iron-based superconductors [34]. The electron cloud shapes of two selected orbitals after Peierls transition are visualized in Figs. 4(b) and 4(c), respectively, and their summation is shown in Fig. 4(d). Correspondingly, the b/a ratio is only 1.576, 9% shorter than the original 1.732 of the highly symmetric one. In other words, the ferroelasticity is superior in the Mg-intercalated case. In short, the physical effects of Mg intercalation are qualitatively similar to the Li intercalation, due to the large electron capacity of multiple orbitals.

Finally, it should be noted that the electron doping effects should not be seriously dependent on the position of intercalation, since here they are only electron donors. Other possible intercalation sites, if they exist, will not alter the emergent results revealed above. Experimentally, the intercalation or adsorption is a common experimental technique in low-dimensional materials studies [35,36].

In conclusion, a 2D f-electron magnet GdI$_3$ and its intercalated variants have been theoretically studied, which exhibit interesting physical properties. First, the pristine GdI$_3$ monolayer can be easily exfoliated from its vdW bulk. Its magnetic ground state is the simplest Néel-type antiferromagnetism. Second, the half- or one-electron doping can be achieved via Li or Mg intercalation, which drives the significant Peierls transition and changes the magnetic ground state. Other emergent physical issues, including ferroelasticity, multiferroicity, as well as magnetoresistivity, are predicted, all of which are expected to be experimentally verified in the near future.

[1] C. Gong and X. Zhang, Science **363**, eaav4450 (2019).

[2] M. An and S. Dong, APL Mater. **8**, 110704 (2020).

[3] M. Wu and P. Jena, Wiley Interdiscip. Rev.: Comput. Mol. Sci. **8**, e1365 (2018).

[4] X. Tang and L. Kou, J. Phys. Chem. Lett. **10**, 6634 (2019).

[5] S. Zhou, L. You, H. Zhou, Y. Pu, Z. Gui, and J. Wang, Front. Phys. **16**, 13301 (2021).

[6] M. A. McGuire, Crystals **7**, 121 (2017).

[7] J.-J. Zhang, L. F. Lin, Y. Zhang, M. Wu, B. Yakobson, and S. Dong, J. Am. Chem. Soc. **140**, 9768 (2018).

[8] R. Hidalgo-Sacoto, R. I. Gonzalez, E. E. Vogel, S. Allende, J. D. Mella, C. Cardenas, R. E. Troncoso, and F. Munoz, Phys. Rev. B **101**, 205425 (2020).

[9] M. A. McGuire, V. O. Garlea, S. KC, V. R. Cooper, J. Yan, H. Cao, and B. C. Sales, Phys. Rev. B **95**, 144421 (2017).

[10] Q. Sun and N. Kioussis, Phys. Rev. B **97**, 094408 (2018).

[11] N. Ding, J. Chen, S. Dong, and A. Stroppa, Phys. Rev. B **102**, 165129 (2020).

[12] S. Y. Kim, T. Y. Kim, L. J. Sandilands, S. Sinn, M.-C. Lee, J. Son, S. Lee, K.-Y. Choi, W. Kim, B.-G. Park *et al.*, Phys. Rev. Lett. **120**, 136402 (2018).

[13] C. Huang, Y. Du, H. Wu, H. Xiang, K. Deng, and E. Kan, Phys. Rev. Lett. **120**, 147601 (2018).

[14] X. Yu, X. Zhang, Q. Shi, S. Tian, H. Lei, K. Xu, and H. Hosono, Front. Phys. **14**, 43501 (2019).

[15] C. Liao, Y. Jin, W. Zhang, Z. Zhu, and M. Chen, Chin. Phys. Lett. **37**, 107505 (2020).

[16] M. J. Coak, S. Son, D. Daisenberger, H. Hamidov, C. R. Haines, P. L. Alireza, A. R. Wildes, C. Liu, S. S. Saxena, and J.-G. Park, npj Quantum Mater. **4**, 38 (2019).

[17] H.-P. You, N. Ding, J. Chen, and S. Dong, Phys. Chem. Chem. Phys. **22**, 24109 (2020).

[18] B. Wang, X. Zhang, Y. Zhang, S. Yuan, Y. Guo, S. Dong, and J. Wang, Mater. Horiz. **7**, 1623 (2020).

[19] G. Kresse and J. Furthmüller, Phys. Rev. B **54**, 11169 (1996).

[20] J. P. Perdew, K. Burke, and M. Ernzerhof, Phys. Rev. Lett. **77**, 3865 (1996).

[21] A. I. Liechtenstein, V. I. Anisimov, and J. Zaanen, Phys. Rev. B **52**, R5467 (1995).

[22] P. Larson, W. R. L. Lambrecht, A. Chantis, and M. van Schilfgaarde, Phys. Rev. B **75**, 045114 (2007).

[23] S. Grimme, J. Comput. Chem. **27**, 1787 (2006).

[24] X. Gonze and C. Lee, Phys. Rev. B **55**, 10355 (1997).

[25] A. Togo and I. Tanaka, Scr. Mater. **108**, 1 (2015).

[26] K. Persson, Materials data on TbI$_3$ (SG:194) by Materials Project (2016), https://materialsproject.org/.

[27] See Supplemental Material at http://link.aps.org/supplemental/10.1103/PhysRevB.103.L161408 for more DFT results.

[28] L. Asprey, T. Keenan, and F. Kruse, Inorg. Chem. **3**, 1137 (1964).

[29] M. An, Y. Zhang, J. Chen, H.-M. Zhang, Y. Guo, and S. Dong, J. Phys. Chem. C **123**, 30545 (2019).

[30] E. Dagotto, Science **309**, 257 (2005).

[31] M. Wu and X. C. Zeng, Nano Lett. **16**, 3236 (2016).

[32] D. V. Efremov, J. van den Brink, and D. I. Khomskii, Nat. Mater. **3**, 853 (2004).

[33] G. Dong, S. Li, M. Yao, Z. Zhou, Y.-Q. Zhang, X. Han, Z. Luo, J. Yao, B. Peng, Z. Hu, H. Huang, T. Jia, J. Li, W. Ren, Z.-G. Ye, X. Ding, J. Sun, C.-W. Nan, L.-Q. Chen *et al.*, Science **366**, 475 (2019).

[34] R. Yu and Q. Si, Phys. Rev. B **96**, 125110 (2017).

[35] J. Zhang, A. Yang, X. Wu, J. van de Groep, P. Tang, S. Li, B. Liu, F. Shi, J. Wan, Q. Li *et al.*, Nat. Commun. **9**, 5289 (2018).

[36] Y. J. Yan, M. Q. Ren, H. C. Xu, B. P. Xie, R. Tao, H. Y. Choi, N. Lee, Y. J. Choi, T. Zhang, and D. L. Feng, Phys. Rev. X **5**, 041018 (2015).